Performance-Tunable Thermal Barrier Coating for Carbon Fiber-Reinforced Plastic Composites via Flame Spraying

Heejin Kim[1+], Kandasamy Praveen[1+], Min Wook Lee[1*], Juhyeong Lee[2*]

[1] Institute of Advanced Composite Materials, Korea Institute of Science and Technology,
Chudong-ro, Bongdong-eup, Jeonbuk, 55324, Republic of Korea
[2] Department of Mechanical and Aerospace Engineering, Utah State University, Logan, UT
84322-4130, USA

[*]Corresponding authors:

Min Wook Lee (mwlee0713@kist.re.kr) and Juhyeong Lee (juhyeong.lee@usu.edu)

[+] Equal contribution

Abstract

Thermal barrier coatings (TBCs) are essential for improving the heat resistance of materials operating in high-temperature environments. This paper proposes a new method for manufacturing double-layered TBC with graded porosity for carbon fiber-reinforced plastic (CFRP) composites. The TBC was created by a flame spraying process, consisting of relatively dense and porous layers: (1) a dense layer was produced by spraying yttria-stabilized zirconia (YSZ) particles directly onto neat carbon fabric substrate and (2) a porous layer was prepared by co-spraying YSZ particles with sacrificial polyetheretherketone (PEEK) particles. The porosity of the porous layer was controlled by varying a PEEK injection distance (D) and a PEEK feed rate (R). The correlation between porosity and thermal conductivity of the TBC layer was investigated to assess its thermal barrier performance. The TBC fabricated with D = 5 cm and R = 1.0 g/min offered the optimal porosity and thermal conductivity. The 660-μm-thick TBC with 34% porosity and 0.27 W/m·K thermal conductivity protected the CFRP substrate remarkably under the subjected torch at 500°C, as the TBC layer reduced the surface temperature of CFRP to 230°C. Thermomechanical analysis, following thermal shock tests, revealed that the double-layered TBC/CFRP composite retained 87% and 75% of its pristine flexural strength and modulus, respectively, while the neat CFRP composite was completely burnt out. This study explored the application of flame spray technology to develop highly effective double-layered TBCs with tunable porosity to maximize their thermal barrier performances. All results from the current study provide new insights into the design and development of TBC and CFRP composites, which will benefit a wide range of lightweight high-temperature applications.

Keywords: Carbon fiber-reinforced plastic (CFRP) composite; thermal barrier coating (TBC); porosity; thermal conductivity; thermal resistivity

1. Introduction

Carbon fiber reinforced plastic (CFRP) composites have been extensively used in aerospace, automotive, and energy industries due to their excellent strength/modulus-to-weight ratio [1-3]. The Airbus A350, the first aircraft whose fuselage and wing structures are made of CFRP, recently crashed at Haneda International Airport. Despite the ensuing fire (above 2000°C [4, 5]), the CFRP fuselage and wing structures delayed the spread of flames and heat transfer into the cabin for up to 90 seconds, preventing casualties and allowing facilitating crew and passengers to evacuate [6, 7]. However, the aircraft eventually combusted completely, highlighting the poor thermal instability of thermoset polymers (i.e., bismaleimide, epoxy, and vinyl ester); these polymers are flammable and begin to decompose at ~330°C [8]. As in the example above, the low thermal stability of polymer matrix composites (PMCs) poses a critical challenge that limits their applications under extreme environments. This is in contrast to metal matrix composites (MMCs) and ceramic matrix composites (CMCs), which can operate at high temperatures (typically exceeding 1000°C [9-11])

CFRP composites for high-temperature applications require thermal barrier coatings (TBCs) that provide significant thermal gradients and dissipate heat, extending their lifetime in high-temperature environments [12-14]. Conventional TBCs are commonly applied to metallic substrates and manufactured by electron-beam physical vapor deposition (EB-PVD), chemical vapor deposition (CVD), and thermal spraying [15]. Among the aforementioned techniques, thermal spraying is widely preferred owing to its simplicity, short processing time, and high scalability for large-scale applications. The fundamental mechanism of thermal spray coating is that particles that are molten or partially molten by heat are accelerated using gas flow to collide with the substrate and solidify, where they rapidly solidify to form a robust mechanical bond [16-18]. Flame spraying, one of thermal spray coating methods, uses the combustion heat of mixed gases, reaching temperatures of up to 3,000°C, to melt the coating particles [19]. Flame spraying has a relatively lower flame temperature than wire arc spraying and air plasma spraying, each reaching temperatures of 4,000°C and 12,000°C [20-22]. The lower flame temperature reduces dramatically with distance from the torch, making it suitable for polymer fabrics including carbon fabric (CF) [23]. In addition, this method offers exceptional portability and adaptability for manual operation, facilitating the coating of complex-shaped substrates.

During thermal spray coating, TBC microstructure can be controlled by adjusting various parameters, including the particle size and shape of the coating materials, injection rate, spray distance, and angle between the spray machine and the substrate [24-26]. TBCs are typically studied at porosity levels of up to ~15% to preserve their mechanical and anticorrosion properties at high temperatures [27]. However, researchers have recently explored deliberately controlling the pores of TBCs to reduce their thermal conductivity and investigate the impact of pore size, shape, and distribution on TBC properties because the pores can effectively reduce thermal conductivity [28, 29]. Bowen et al. [30] demonstrated that graded porous TBCs, with porosity decreasing from top to bottom, exhibit lower thermal conductivity and improved delamination resistance compared with specimens with uniform porosity distributions. Several studies have been conducted to study the thermal performance of CFRP composites and suggest materials solutions to improve their high-temperature performance. Suryanarayanan et al. [31] fabricated aerogel-protected CFRP composites via a repetitive dip coating process. At 100°C, a 700 μm-thick aerogel/epoxy coating layer reduced the back-surface temperature of a CFRP specimen by ~50°C. Laungtriratana et al. [32] fabricated glass fiber-reinforced polymer (GFRP) composites using the hand lay-up method with post-curing at 80°C for 6 hr, incorporating a thin phenolic coating layer with various ceramic particles (nano clay, glass flakes, Si, Al_2TiO_5, ZrO_2). They also added additional sieved ceramic particles before the curing of the phenolic coating and then co-cured at room temperature for 12 hr and 80°C for 24 hr. When a heat flux of 35 kW/m^2 was applied, the time needed by the back-surface temperature of the GFRP specimens covered with sieved Al_2TiO_5 particles to reach 180°C and 250°C increased by 49 s and 63 s, respectively, compared with those of the control sample (a GFRP specimen without a ceramic coating layer); this time delay indicates the materials' improved thermal endurance. Golewxki et al. [33] used an alumina (Al_2O_3) fiber mat with an epoxy resin binder as a TBC layer for CFRP composites. Ceramic mat/CFRP specimens were manufactured in an autoclave by laminating the ceramic mat on CFRP prepregs and then impregnating an uncured epoxy binder resin. A 5 mm alumina TBC layer reduced the back surface temperature of the CFRP specimen to 150°C when subjected to 800°C for 1 min. However, the TBC layer was damaged due to the thermal decomposition of the epoxy binder. Fabrizia et al. [34] used a 62 μm thick graphene nanolayered film as a TBC, which was then co-cured with CF prepregs. When heated by a laser at 100 kW/m^2, the surface temperature reached approximately 520°C, and after passing through a 1.7 mm thick CFRP, the temperature was about 220°C. However, the coating layer's swelling and the CFRP delamination were observed. Ju et al. [35] fabricated a carbon nanotube (CNT)-reinforced ceramic TBC layer by polymer infiltration and pyrolysis (PIP) and co-cured with the carbon fiber/bismaleimide (BMI) composite substrate. The TBC containing CNTs exhibited excellent structural integrity and high-temperature tolerance but showed considerable weight loss (~24%, when subjected to >610°C) owing to BMI's thermal oxidation/decomposition. As well known in the open literature, the PIP process is performed under high-temperature and high-vacuum conditions, leading to lengthy durations, size limitations, and expensive manufacturing costs [36]. Our previously published paper [37] proposed a porous Al_2O_3-based TBC layer for CFRP composites. The TBC's porous structure formed mechanical interlocking through epoxy branches, increasing adhesion with the CFRP composite substrate and providing improved thermal barrier performance by reducing the overall thermal conductivity of the TBC layer. When the TBC/CFRP composite specimens were exposed to 500 – 700°C flame for 10 min, a 1.45 mm-thick Al_2O_3-based TBC remarkably reduced the CFRP specimens' surface temperatures to 188 – 228°C.

The paper aims to fabricate a non-flammable TBC layer for the CFRP substrates to protect them against high temperatures. Flame spraying was conducted to fabricate a yttria-stabilized zirconia (YSZ)-polyetheretherketone (PEEK) hybrid double-layered TBC on a desized CF substrate. A YSZ-PEEK hybrid double-layered TBC layer was manufactured on the dry CF; a dense YSZ layer was first flame-sprayed on a desized dry CF, followed by the co-spraying of PEEK powder to form a YSZ-PEEK layer. The PEEK material was subsequently removed via heat treatment to create pores. The porosity of a YSZ-PEEK layer was controlled by adjusting the PEEK injection distance (D) and the PEEK feeding rate (R). The optimal porosity levels, balancing the thermal conductivity and mechanical properties of the TBC, were controlled through adjustments in the flame spraying parameters. The double-layered TBC/CFRP composite was manufactured via two-step curing: the pre-curing of the CFRP substrate and post-curing for combining the TBC and CFRP. Thermal shock tests at 500°C for 10 min demonstrated that the 660-μm-thick TBC layer reduced the surface temperature of the CFRP to approximately 230°C, providing effective thermal protection performance. Subsequent flexural tests on the TBC/CFRP specimens subjected to 500°C showed 13% strength degradation and 25% modulus degradation compared with the control specimen. This paper aims to provide new insight into designing and developing an effective hybrid TBC layer with graded porosity, which will benefit a wide range of CFRP composite applications in extreme conditions.

2. Materials and experimental process

2.1. *Materials*

The ceramic powder materials typically used for TBCs require high melting temperatures, low thermal conductivity, and mechanical endurance to retain their mechanical integrity at their operating temperatures [38-40]. YSZ powder is a common TBC ceramic powder that has a melting point of 2,700°C[41, 42], thermal conductivity of 1.5–2.5 W/m·K at 25°C–1,000°C [43], and remarkable strength and toughness. In this study, 7–8 wt% YSZ powder (Sewon Hardfacing Co. Ltd., South Korea) was used as a backbone of double-layered TBC. PEEK (Victrex, UK) was used as a pore-forming material that control porous structure by decomposing during the heat treatment after being sprayed with YSZ. The 3K plain-woven CFs (T300, 200 g/m^2, Toray, Japan) with sizing treatment were used as the TBC substrate and underlying CFRP composite. An unmodified, medium viscosity liquid epoxy resin (YD 128, Epotec, USA) derived from bisphenol-A, a reactive butyl glycidyl ether (BGE, Kukdo Chemicals, Korea) diluent, and a polyamide hardener (G-640, Kukdo Chemicals, Korea) were used as matrix.

2.2. *Specimen Fabrication*

The TBC layer was fabricated as a double-layered structure on a dry plain-woven CF substrate using the flame spraying process (Fig. 1a). Prior to the flame spraying, the CF substrate was subjected to a meticulous manual rubbing process in an acetone bath to remove the sizing agent. This process rearranges inter yarn pores in the open-structured woven CF by spreading individual carbon fibers within a tow. After the desizing treatment, open pores in the fabric can be eliminated, providing a dense coating layer without discontinuities in the TBC layer. To ensure a stable CF substrate without wrinkles caused by the high-velocity flame during flame spraying, a frame-shaped steel guide (inner cut-out dimensions 60 × 60 mm^2) was used as the holder. A dense YSZ layer was first coated on the desized CF substrate via flame-spraying YSZ powders. The PEEK was then co-sprayed with YSZ on the dense layer, creating an additional YSZ–PEEK coating layer. Flame spraying was conducted using a flame spray gun (CastoDyn DS8000, Eutectic Korea Ltd., Korea) operating at an oxygen and acetylene pressure of 4 MPa and 0.12 MPa, with a corresponding gas flow rate of 7.5 m/s and 1.3 m/s, and ignited by lighter. These conditions, identified through preliminary experiments, represent the optimal process parameters determined during flame spraying. All the coating processes were performed using a raster pattern (Fig. 1b) with an overlap of 5 mm. The number of coating passes was determined to ensure complete coverage and uniform thickness of the entire area of the desized CF. The standoff distance (D_s) between the CF substrate and flame gun was fixed at 14 cm, while the horizontal substrate moving speed (V_s) was set to 550 mm/min. All parameters for fabrication of double-layered TBC used in the present study are summarized in Table 1. An approximately 207-µm-thick dense YSZ layer was formed by four passes of flame-spraying coating over the plain-woven CF substrate. Subsequently, the YSZ-PEEK layer was overlaid with a thickness of 250–580 µm, based on the co-splaying conditions D and R in Fig. 1a, both of which were variables to control the microstructure of a porous TBC layer. During flame coating, the CF substrate was cooled down at room temperature, and every two coatings passed to avoid potential damage to the CF substrate.

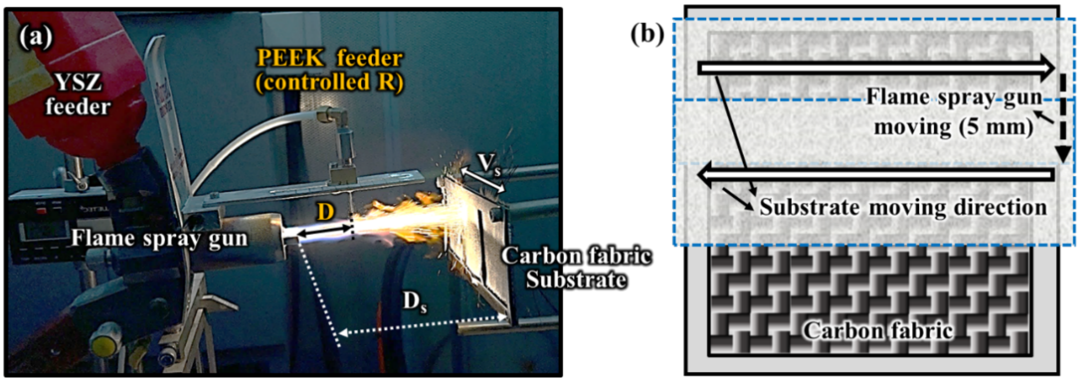

Figure 1. (a) Experimental setup of flame spraying and (b) coating pattern.

Table 1. Fabrication parameters of double-layered TBC

Parameter	Value
Pressure of O_2 (MPa)	0.40
Pressure of C_2H_2 (MPa)	0.12
Standoff distance (D_s, cm)	14
Substrate moving speed (V_s, mm/min)	550
Substrate dimensions (mm^2)	600 × 600
Number of coating passes for the dense layer	4
Number of coating passes for the porous layer	6
Distance between the flame spray gun and PEEK feeder (D, cm)	2/5/8
PEEK feed rate (R, g/min)	0.8/1.0/1.3
Temperature of heat treatment for PEEK degradation (°C)	500
Time of heat treatment for PEEK degradation (h)	5

After flame spraying, the double-layered TBC coated CF substrate was subjected to heat treatment at 500°C for 5 hr to decompose the PEEK particles in the YSZ-PEEK layer (Fig. 2). This heat treatment transformed the PEEK-occupied volumes into pores, thus forming a porous YSZ layer.

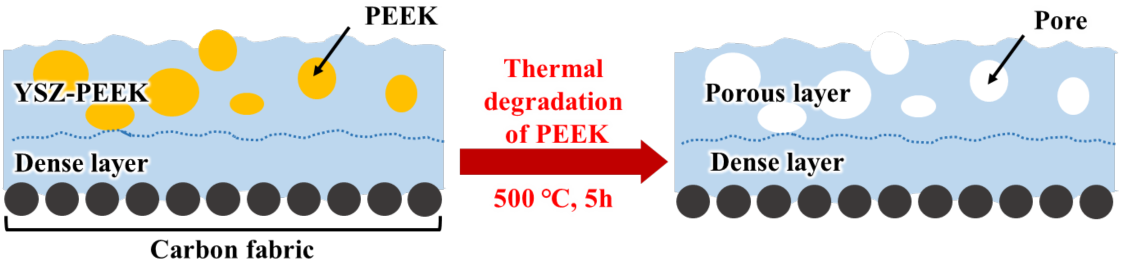

Figure 2. Schematic of double-layered TBC fabrication.

The TBC/CFRP composites were manufactured by the vacuum-assisted resin transfer molding (VARTM) process (Fig. 3). The YD 128 epoxy resin and reactive BGE diluent were mixed in a 9:1 weight ratio to promote resin impregnation during the VARTM process. The G-640 polyamide hardener was then added with the epoxy-diluent mixture in a 10:6.4 weight ratio, followed by degassing for 30-40 min. 12 plain-woven CFs were partially cured by the epoxy-diluent–hardener mixture at 80°C for 30 mins (Fig. 3a). The TBC-coated CF, fabricated with D = 5 cm, R = 1.0 g/min, was then placed on top of the partially-cured laminated woven fabric composite. The TBC/CFRP composite was then co-cured according to the manufacturer's recommendation (80°C for an additional 3.5 hr [44]), as shown in Fig. 3b.

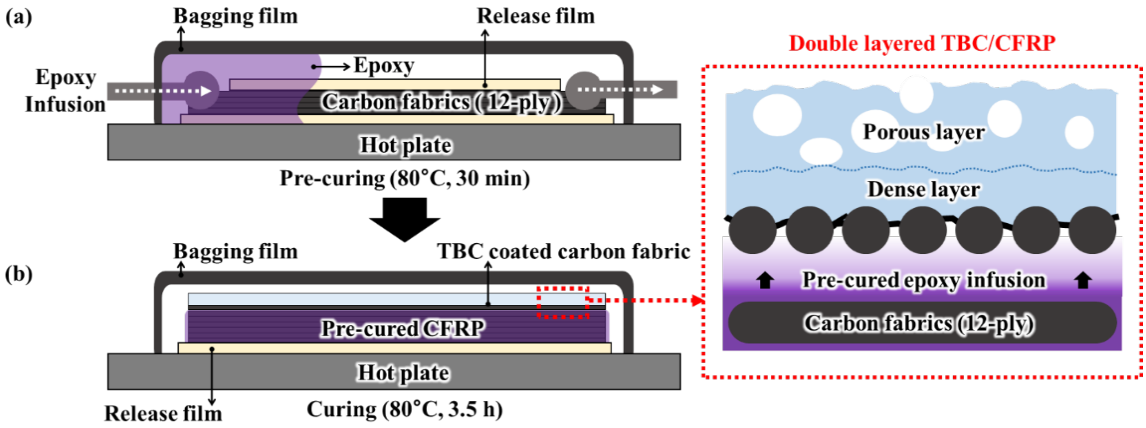

Figure 3. Schematic of TBC/CFRP composite manufacturing process: (a) Precuring process of the CFRP substrate and (b) Post-curing of the TBC/CFRP composite.

2.3. Material Characterization

Scanning electron microscope (SEM, Verios, Nano SEM 460; FEI, USA) and optimal microscope (OM, VHX-900 F, Keyence Corporation, Japan) were used to observe key microstructure features, including the YSZ, PEEK, and corresponding pore fractions within the TBC layer. The particle size distribution, porosity and thickness of the porous TBC layer were analyzed using ImageJ software on the SEM and OM images. Porosity was analyzed from at least 10 different cross-sectional images, and thickness was measured at more than 100 points. The composition of the TBC was investigated using an energy-dispersive X-ray (EDX) spectrometer. The porous specimen density was calculated using the Archimedes method, and the bulk and apparent densities were calculated using Eqns. (1) and (2) following ASTM C373 [45]:

$$\text{Bulk density } (\rho_b) = \frac{m_s}{(V_s+V_c+V_o)} = \frac{W_d}{W_w - W_s}. \tag{1}$$

$$\text{Apparent density } (\rho_a) = \frac{m_s}{(V_s+V_c)} = \frac{W_d}{W_d - W_s}. \tag{2}$$

where m_s represents the weight of the sample, and V_s, V_c, and V_o represent the true volume, captured pore volume, and open pore volume of the sample, respectively. Alternatively, the density can be calculated by measuring the dry weight W_d, wet weight W_w, and soaking weight W_s. In this work, the W_s was determined by immersing the sample in distilled water at room temperature for a minimum of 3 hr. The bulk density (Eqn. 1) represents the density considering the volume of open pores, differing from the apparent density (Eqn. 2) which includes only internal pores. Each density is measured based on weight, thus can be used to calculate actual open pore fraction in the total pore volume, as follows:

$$P_{open} = \frac{V_o}{V_s+V_c+V_o} \times 100 = \left(1 - \frac{\rho_b}{\rho_a}\right) \times 100 \tag{3}$$

Thermal diffusivities of the TBC, CFRP substrate were measured within the temperature range of 25 – 400°C using laser flash analysis (LFA) (LFA 467, Netzsch, Germany) at least three times. To measure the thermal conductivity of the pure TBC and compare the porosity effect, the CF substrate used in the flame spraying process needed to be removed. This was achieved by treating the samples in a furnace at 800°C for 3 hr to ensure complete removal. Specific heat, ranging from 0°C to 450°C at a rate of 10 °C /min, was analyzed using DSC (DSC 214 Polyma Netzsch, Germany) three times with approximately 12 mg of the sample, and thermal conductivity was calculated using Eqn. 4.

$$\lambda = \alpha \times \rho \times C_p \tag{4}$$

where λ represents the thermal conductivity. α, ρ, and C_p represent the thermal diffusivity, density, and specific heat, respectively. In this study, the ρ_b considering open pores and internal pores were used as ρ (see Table S1 and S2).

2.4. Thermal Shock Tests

Figure 4 shows a schematic of the thermal shock test setup for evaluating the thermal barrier performance of the TBC/CFRP composite, as presented in our previously published study [37]. Thermal shock tests were performed using a methane gas burner with an 11 mm diameter for 10 min. To prevent direct contact of the flame with the upper surface and edge side of the specimens, the pristine CFRP and TBC/CFRP specimens were each dimensioned to 50 mm × 50 mm × 2.98 mm and 50 mm × 50 mm × 3.66 mm thickness. These specimens were tested at least five times. Each specimen was clamped at a distance above the burner, and the flame temperature T_H was controlled by adjusting the distance between the burner and the specimen. For the thermal shock test at T_H = 500°C considered in the present study, the specimens were 2.3 cm away from the methane gas burner. The methane gas flow rate was fixed at 115 cm^3/min. The surface temperature of the CFRP substrate (T_{CFRP}) was carefully measured using an infrared (IR) thermal imaging camera (T62101, FLIR). The angle and distance between the specimen and the IR thermal imaging camera were 30° and 500 mm, respectively. The emissivity of the CFRP specimen was set to 0.96 in the IR thermal imaging camera. More details on thermal shock test configuration and procedure can be found in the reference [37].

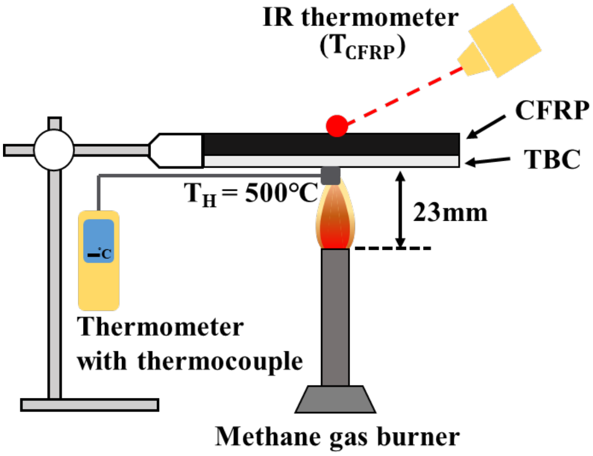

Figure 4. Schematic of the thermal shock test.

2.5. Mechanical test

Three-point flexural bending tests were performed at least three times for each material/test configuration, according to ASTM D790 [46], to characterize the failure mechanisms of the TBC/CFRP composite specimens after thermal shock. The three-point bending tests were conducted using a universal test machine (Instron 4464, Instron, USA). After the thermal shock test, the TBC/CFRP specimens with in-plane dimensions of 50 mm × 50 mm were trimmed to 50 mm × 12.7 mm using a waterjet cutter, retaining only the central portion. The specimens with thermally shocked region were tested at a crosshead speed of 1 mm/min with a span length of 40 mm. Various damage modes, including delamination, matrix cracks, and matrix thermal decomposition in the TBC/CFRP specimens were investigated using OM images. The tensile adhesion/bonding strength of the TBC to the CFRP substrate was evaluated. The tensile adhesion test was performed using a universal tensile testing machine (TOFO-330R6, TOFO, Republic of Korea) at a 1 mm/min speed according to ASTM C633 [47]. The TBC/CFRP specimens were attached to a 2.5 mm × 2.5 mm rectangular fixture using an epoxy adhesive (DP460, 3M, USA). The TBC layer of the specimens was ~ 0.66 mm thick dense YSZ layer, considering the possibility of adhesive penetration through porous YSZ layer.

3. Result and discussions

3.1. Flame-Sprayed TBC

Figures 5a and 5b show the particle shape and size distributions of YSZ and PEEK powders, respectively. The size of YSZ particles was determined based on their diameter, while that of PEEK particles was determined based on the longest length between their vertices. YSZ powders were spherical with a 25 μm average diameter and showed a relatively narrow size distribution. In contrast, PEEK powders showed irregular shapes with a wide particle size distribution ranging from 9 to 135 μm.

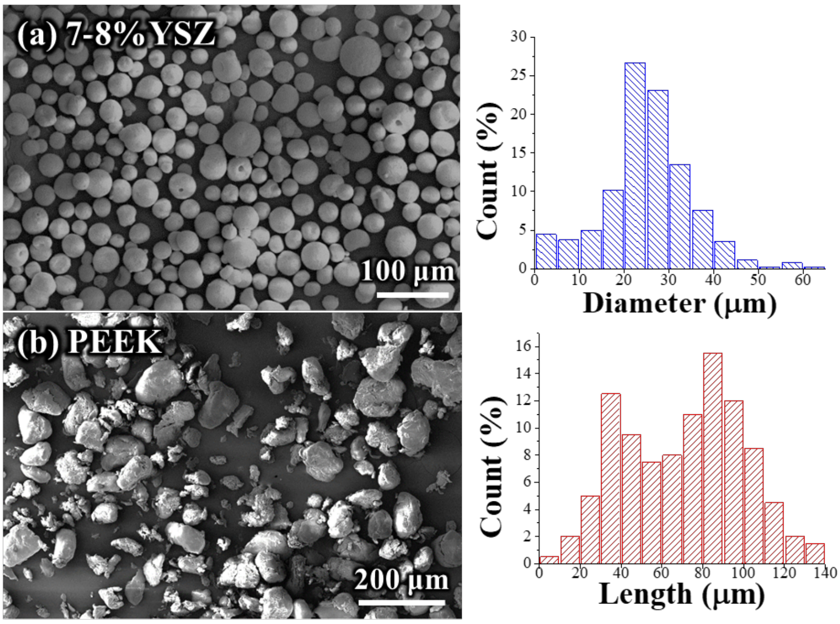

Figure 5. SEM images and particle size distribution of (a) YSZ (used as a thermal barrier material) and (b) PEEK (used as a pore-forming agent).

The flame spraying process for producing a YSZ coating poses difficulties. These difficulties can be attributed to the use of an acetylene–oxygen mixture during this process, which can achieve a maximum heating temperature of only ~3,000°C. This temperature is insufficient to rapidly melt YSZ particles because of the low residence time of these particles in the flame stream. Therefore, achieving uniform YSZ coating on CF substrate is challenging [48, 49]. Therefore, during a preliminary experimentation step, several adjustments were made to identify key process parameters, including the D_s, V_s, and the flow rate of gases for YSZ flame spraying. Notably, the acetylene gas flow rate emerged as the most influential parameter in achieving a uniform YSZ coating on the desized CF; the flame spraying conditions considred in this work are presented in Table 1.

Figure 6 shows the effect of the desizing of the neat CF on the TBC layer. Remarkably, the pristine TBC layer (Fig. 6a) shows multiple holes sized dimensions of 480 μm × 568 μm at the warp–weft intersection of the neat CF even after the YSZ coating. During the TBC/CFRP composite manufacturing process, epoxy resin can be infused to fill these holes, and it can potentially ignite when exposed to high temperatures. In contrast, the acetone-treated CF (Fig. 6b) exhibits a continuous surface with fiber tow width ranging from 1.4 to 1.8 mm without visible open holes after YSZ coating.

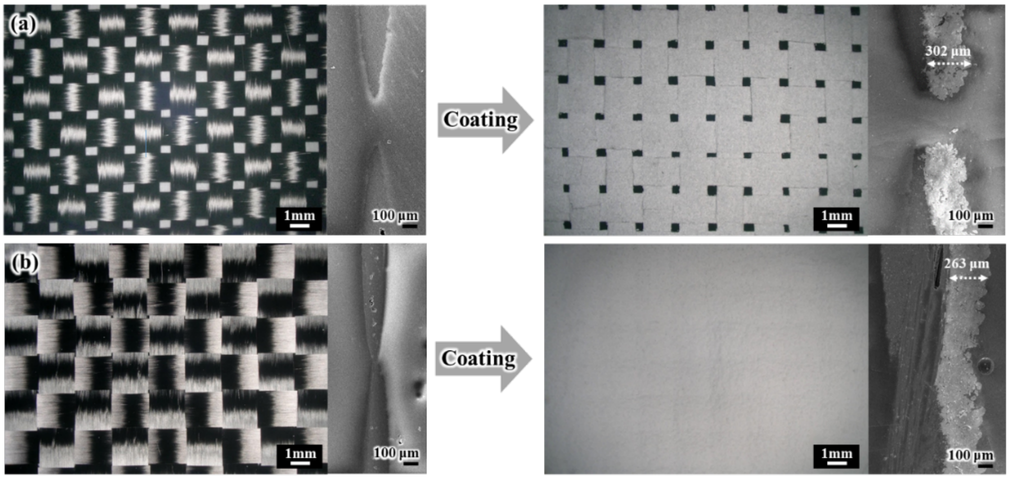

Figure 6. Effect of desizing on TBC surface morphology: (a) pristine and (b) desized CF substrates. (only YSZ particles were flame sprayed for four passes with D_s = 14 cm).

For heat shielding, thermal conductivity should be kept low to prevent external heat sources from transmitting inward [50]. The thermal conductivity of the TBC layer can be tuned by controlling its microstructure. An increase in TBC's porosity is one of the most effective parameters that reduce its overall thermal conductivity. In this work, the PEEK powders were co-sprayed as a sacrificial material with YSZ powders to fabricate the YSZ-PEEK layer as a pre-stage of the porous TBC layer. Note that the PEEK was chosen because of its high thermal degradation temperature (500-700°C), which can withstand exposure to high-temperature flame stream during spraying without burning out completely. The PEEK powders present within the YSZ-PEEK layer were selectively removed at a temperature lower than the melting temperature of YSZ (2,700°C) but at an initial decomposition temperature of PEEK (~500°C). After this heat treatment, the areas pre-occupied by PEEK powders were then left empty and porous YSZ microstructure can be formed. The black regions on the YSZ-PEEK layer surface (Fig. 7a) indicated partial thermal degradation of PEEK. The black regions darkening from top to bottom were attributed to the movement of the flame-spraying gun. During repeated coating passes, the previously coated PEEK was thermally degraded (turning black) and gradually removed by the flame stream, transforming into white areas. The SEM images shown in Fig. 7a reveal thermally damaged PEEK particles (yellow arrows) adhered between YSZ splats at the TBC surface and cross-section. Some of the YSZ particles maintained their original spherical shape without complete melting (see the magnified depiction of Fig. 7a surface), supporting the insufficient flame temperature and exposure time for YSZ material to melt. Fig. 7b shows the same layer with all PEEK particles removed, where several pores are clearly observed after heat treatment of CF-coated YSZ-PEEK at 500°C for 5 hr. However, a some of residual PEEK particles is observed in internal pores, as shown in the cross-sectional and EDS mapping images, where red represents carbon (C) from PEEK, and blue represents zirconium (Zr) from YSZ. These pores are more distinctly discernible than in Fig. 7c, where the YSZ coating layer has smoother surface roughness/texture. The observations suggest that all PEEK powders with various sizes can be converted into pores after heat treatment, thus it is feasible to control the overall porosity and thermal conductivity of the YSZ layer.

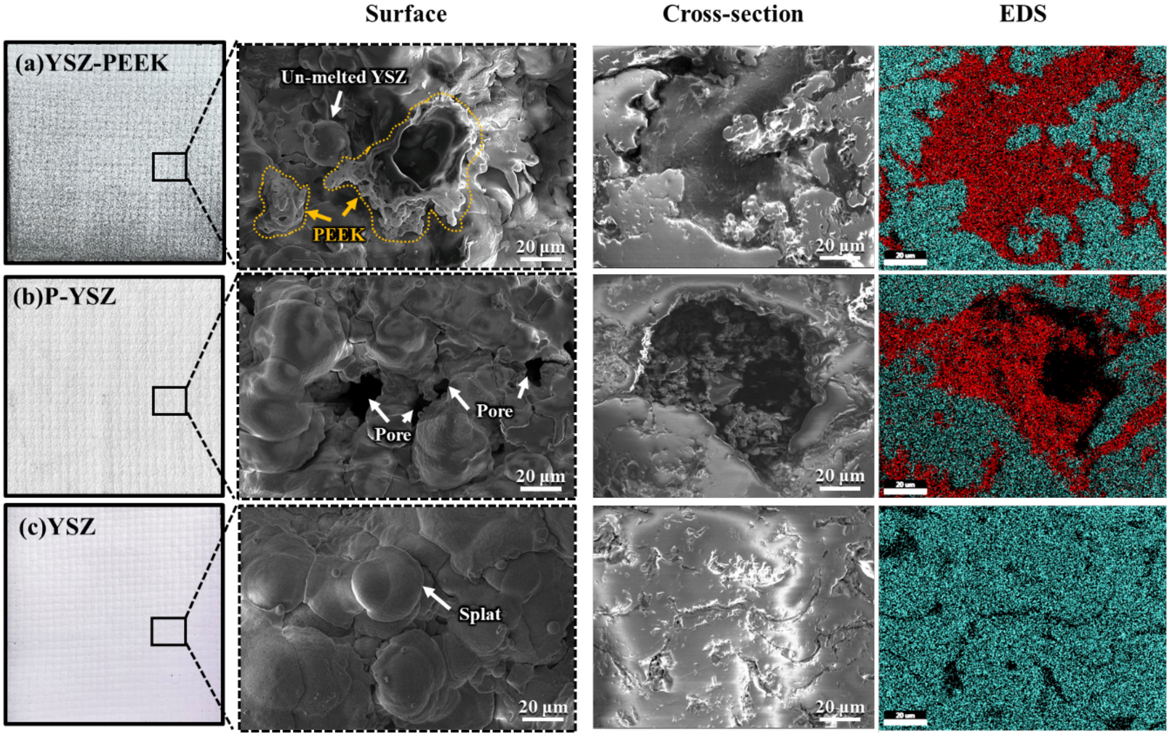

Figure 7. Visual inspection and SEM images and energy-dispersive X-ray element mapping of C (PEEK-red) and Zr (blue) in (a) YSZ-PEEK layer, (b) heat-treated co-sprayed YSZ–PEEK layers (D = 5 cm and R = 1.0 g/min) and (c) sprayed YSZ layer (D_s = 14 cm).

The dense layer of the double-layered TBC plays a crucial role in preventing upstream of the resin during TBC/CFRP composite manufacturing and enables mechanical interlocking with the desized CF. The porous top layer had numerous pores and low thermal conductivity, which helped promote the thermal barrier performance.

Figure 8 shows cross-sectional SEM images of the double-layered TBC layers fabricated with various R, while D was kept as the same (D = 5 cm). The dense layer was produced by flame spraying YSZ under the condition in Table 1, while the porous layer was sprayed with YSZ under the same conditions and PEEK with D = 2, 5, and 8 cm. The TBC-coated CF substrate was heat-treated at 800°C for 3 hr to achieve the free-standing coating and was subjected to thermophysical property measurement. Furthermore, the standard metallographic procedure (mounting, curing, cutting, and polishing the samples down to 1 μm in a colloidal liquid) was conducted to achieve scratch-free microstructural features. The SEM observation (Fig. 8) shows that the dense layer was about 207±16 μm thick in all three coatings, and the porous layer considerably varied in thickness and porosity because of the variation in D. Simiarily, as shown in Fig. 9, the TBC fabricated with various D, while R was kept as the same (R = 1.0 g/min) exihibited a dense layer with comprable thickness and a porous layer with various thickness. In fact, the differences in D and R altered the temperature and velocity of the flame streams because of the inflight PEEK particles, substantially influencing the coating microstructure [51].

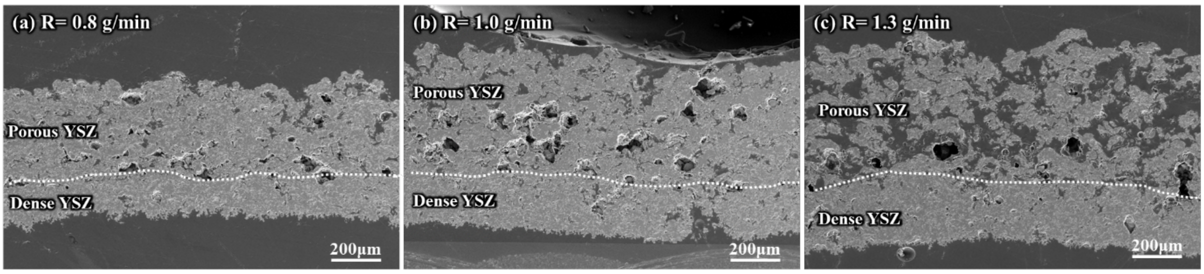

Figure 8. Cross-sectional images of double-layered TBC depending on the PEEK feed rate R (a) 0.8 g/min, (b) 1.0 g/min, and (c) 1.3 g/min (PEEK feed distance D = 5 cm).

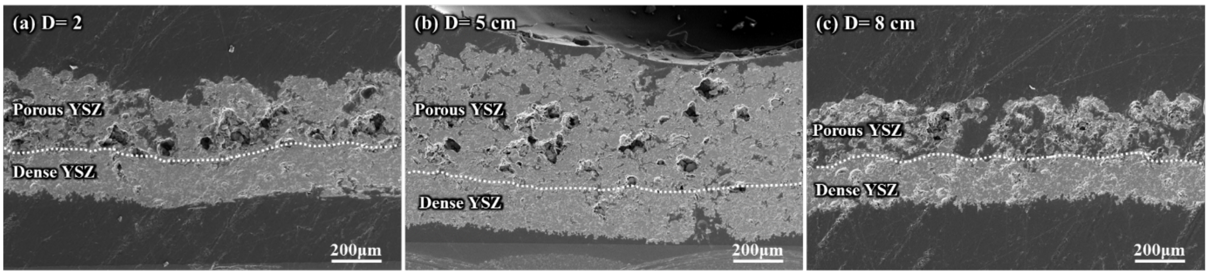

Figure 9. Cross-sectional observation of a double-layered TBC layer fabricated at various PEEK injection distances D: (a) 2 cm, (b) 5 cm, and (c) 8 cm (PEEK feed rate R = 1.0 g/min).

Figure 10 shows the TBC porosity and thickness as a function of D and R. At R = 1.0 g/min and D = 2 cm (Fig. 10a), the flame stream temperature was considerably high, and PEEK underwent thermal decomposition, which burned most of the PEEK particles. This resulted in small pores and low porosity in the coating microstructure. The coating porosity and thickness were approximately 17% and 450 μm, respectively. At the optimal D of 5 cm, the coating showed a porous architecture (~24% porosity) with various pore sizes and shapes, and the coating thickness was ~640 μm. At D of 8 cm, the temperature and velocity of the flame stream were low. The flame temperature was insufficient for melting and burning PEEK, and the momentum toward the coating surface was inadequate; consequently, the coating had a large number of pores and voids and similar sizes and shapes of PEEK particles. At this distance, the PEEK particles disturbed the momentum and direction of the YSZ particles, leading to poor adhesion and interparticle bonding. The coating porosity was more than 32%. Based on this observation, an optimum PEEK injection distance was determined as 5 cm in this work.

According to the microstructural observation, the porosities of the coatings were 19%, 24%, and 33%. An increase in the R gradually increased the coating porosity. The increment in R resulted in poor melting and decreased the velocity of the flame stream because of the vertical injection of PEEK [52].

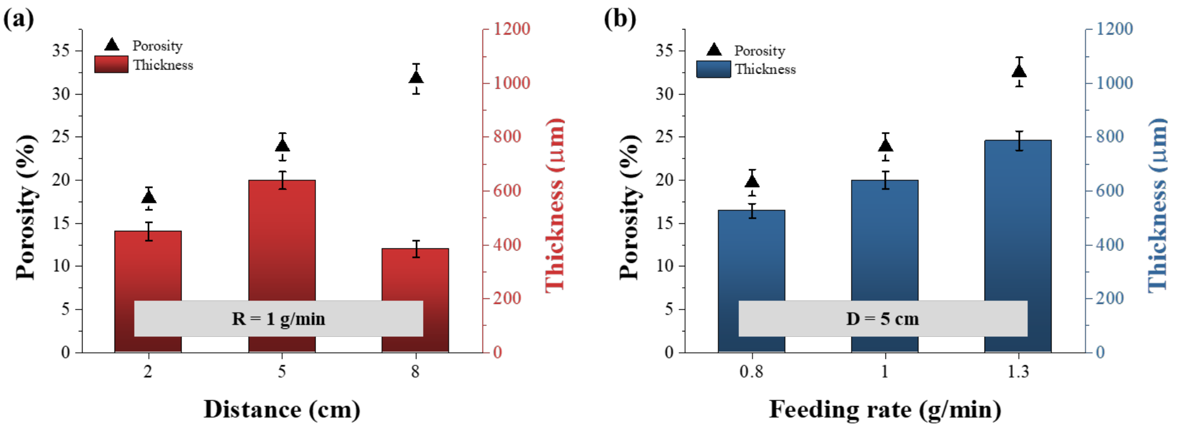

Figure 10. Porosity and thickness of the double-layered TBC as a function of (a) D and (b) R.

As previously discussed, the porosity of a double-layered TBC increased with increasing D and R, which may compromise its structural stability. Increasing R increased the fraction of open pores in the coating microstructure from 32% at 0.8 g/min to 41% at 1.3 g/min, as shown in Table 2. A highly porous TBC was achieved at the 1.3 g/min feed rate. At R = 1.3 g/min, numerous large pores formed by the connection of smaller pores are observed. However, it exhibited fragility and struggled to maintain structural stability, particularly when subjected to vacuum pressure during TBC/CFRP manufacturing. In this work, D = 5 cm and R = 1.0 g/min were found to be the optimal flame spraying parameters for TBC/CFRP manufacturing, achieving improved thermal barrier performance and structural stability. Porosity and thickness measurements of all TBCs used in Fig. 10 are included in Table 2.

Table 2. Bulk and apparent densities, and open pore fraction of TBC frabicated with various D and R.

D (cm)	R (g/min)	Bulk density (g/cm^3)	Apparent density (g/cm^3)	Open pore (%)	Thickness (μm)
2	1.0	4.05 ± 0.19	5.55 ± 0.03	27.02 ± 3.35	449.44 ± 33.86

5	1.0	3.78 ± 0.08	5.68 ± 0.03	31.61 ± 1.89	639.87 ± 32.27
8	1.0	3.55 ± 0.05	5.80 ± 0.00	38.85 ± 0.90	384.48 ± 30.71
5	0.8	3.99 ± 0.14	5.67 ± 0.04	29.48 ± 2.38	526.32 ± 26.79
5	1.0	3.78 ± 0.08	5.68 ± 0.03	31.61 ± 1.89	639.87 ± 32.27
5	1.3	3.33 ± 0.11	5.68 ± 0.04	41.34 ± 2.03	787.33 ± 35.57

3.2. Thermal Conductivity Measurement

Thermal conductivity is the primary factor affecting the thermal barrier performance of TBCs. Low thermal conductivity is preferred to achieve maximum thermal barrier performances. Thermal conductivity was calculated according to Eqn. 4, and the averaged thermal conductivity value was used for the analysis.

Figure 11 shows the temperature-dependent thermal conductivity of the free-standing porous YSZ specimens prepared with various D and R. For all D with R = 0.3 g/min (Fig. 11a), the thermal conductivity of the porous YSZ specimen decreased as temperature increased. Correspondingly, the bulk density at D = 2, 5, and 8 cm decreased and remained consistent at 4.56, 4.39, and 4.39 g/cm^3, respectively. Thermal conductivity results follow a similar trend as density, indicating that thermal conductivity can be tailorable by controlling porosity. Figure 11b shows the thermal conductivity of the TBC fabricated with D = 5 cm and various R. The bulk densities, which follow a similar trend to thermal conductivity, were measured at 4.20, 4.08, and 3.98 g/cm^3. Thermal conductivity measurements of the porous layer show two key findings: (1) thermal conductivity decreases as both D and R increase and (2) thermal conductivity decreases as temperature increases. For instance, room temperature thermal conductivity decreases from 0.54 to 0.44 W/m·K as R increases from 0.8 to 1.3 g/min. A decrease in TBC’s thermal conductivity, resulting from increases in D and R, which was attributed to the increased porosity and voids, as confirmed by the aforementioned microstructural observation (Figs. 9 and 10). The reduction of thermal conductivity with increasing porosity may be attributed to phonon scattering occurring between the splats, as suggested by various studies [53, 54]. However, this research did not directly investigate phonon scattering in the porous TBC layer. Particularly, the decrease in thermal conductivity is notably more pronounced as R increases from 1.0 to 1.3 g/min, primarily owing to the presence of numerous open pores. These open pores effectively reduce the overall thermal conductivity of a porous TBC layer, particularly via convective heat transfer, when a temperature gradient exists between the interior and surface of TBCs [55].

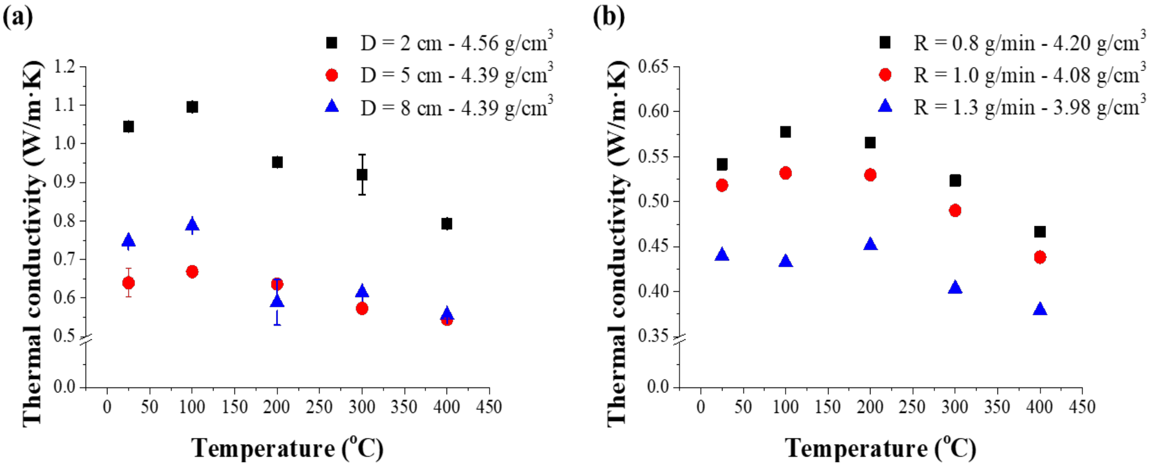

Figure 11. Effects of PEEK feed distance D and rate R on the thermal conductivity of a porous YSZ layers prepared with (a) D = 2–8 cm with R = 0.3 g/min and (b) R = 0.8–1.3 g/min with D = 5 cm.

Figure 12a compares the thermal conductivities of dense TBC, double-layered TBC, and pristine CFRP composite as a function of temperature. The dense YSZ layer (blue) showed thermal conductivity ranging from 1.06 to 1.39 W/m·K between 25°C and 400°C. The double-layered TBC (red) exhibited a nearly constant thermal conductivity of 0.32 W/m·K over the same temperature range. The room temperature thermal conductivity of pristine CFRP composite (black) was approximately 0.55 W/m·K. The relatively low thermal conductivity of a double-layered TBC layer, compared to the underlying CFRP substrate, is suitable for thermal barrier applications. Figure 12b shows the porosity and thermal conductivity of porous YSZ

TBCs fabricated using various methods (electron beam physical vapor deposition (EB-PVD) [42, 56], air plasma spraying (APS) [57-59], suspension plasma spray (SPS) [60, 61]) in the open literature. The microstructure differences of these TBCs resulting from their fabrication methods determine their heat conduction paths, leading to variations in thermal conductivity. In particular, the double-layered YSZ TBC fabricated in this study exhibited considerably lower thermal conductivity compared to conventional TBCs. The lower thermal conductivity was attributed to distinct splat boundaries and numerous unmelted particles in the microstructure, whereas the APS coatings have good mechanical interlocking between splats and have good structural integrity. These characteristics influenced phonon scattering, thereby reducing thermal conductivity [62, 63].

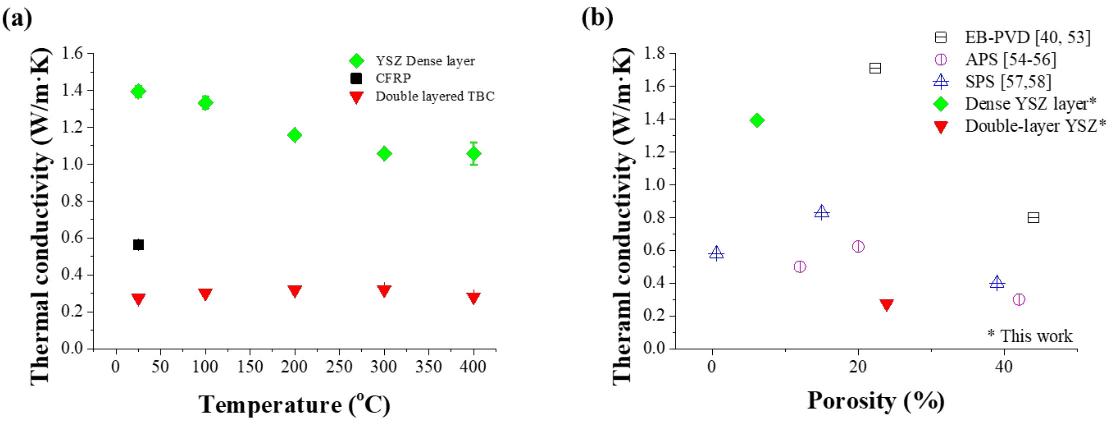

Figure 12. Comparison of thermal conductivity between (a) a TBC/CFRP componentand (b) a porous YSZ coating from other references. (Double layered TBC made with D= 5 cm and R = 1.0 g/min)

3.3. Thermal Shock Test Results

The thermal shock test (T_H = 500°C for 10 min) was conducted to evaluate the thermal performance of pristine CFRP and TBC/CFRP composites, where the TBC was prepared with D = 5 cm and R=1.0 g/min. Figure 13 compares the back-face surface temperature profiles of the CFRP and TBC/CFRP specimens and their corresponding visual inspection. As mentioned earlier, the CFRP and TBC/CFRP specimens were each dimensioned

50 mm × 50 mm × 2.98 mm and 50 mm × 50 mm × 3.66 mm, resulting in a 660 µm-thick TBC layer when excluding a single CF ply (0.02 mm). For the pristine CFRP specimen, the surface temperature reached 300°C after 300 s and started to ignite at the bottom. The flame then continued to spread throughout the specimen owing to the thermal decomposition of the matrix occurring from 300°C [64, 65]. However, the surface temperature of the TBC/CFRP specimen was maintained at 230°C for 10 min, and no auto-ignition and burning were observed. Note that 230°C is lower than the initial thermal decomposition temperature of typical epoxy matrices (~300°C [64, 65]). This result shows that the double-layered YSZ TBC can effectively prevent the underlying CFRP laminate from realistic high-temperature exposures such as volatile fuel combustion temperatures [66, 67] and wildfires [68] in the temperature range of 420 – 600 °C.

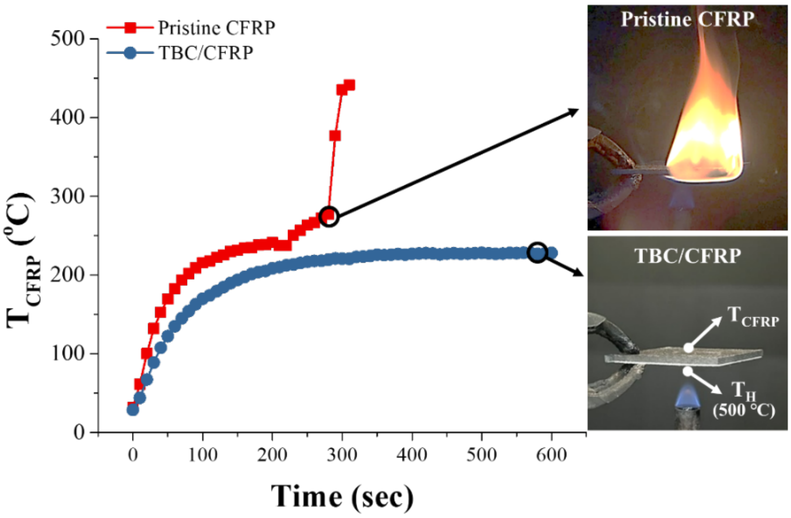

Figure 13. The back-face surface temperature of the CFRP and TBC/CFRP composites during the thermal shock test.

Figures 14a and 14b show the macroscopic views of the thermal-shock-tested pristine CFRP and TBC/CFRP specimens, respectively. Significant delamination was observed in the pristine CFRP specimen due to the thermal decomposition of the epoxy matrix occurring at each interface. In contrast, the TBC/CFRP specimen experienced no physical damage; the coating surface was merely discolored and scorched owing to the residual PEEKs in porous TBC layer. Thus, the double-layered YSZ TBC offered a temperature gradient across the specimen thickness and effectively functioned as a thermally protective layer at high temperatures.

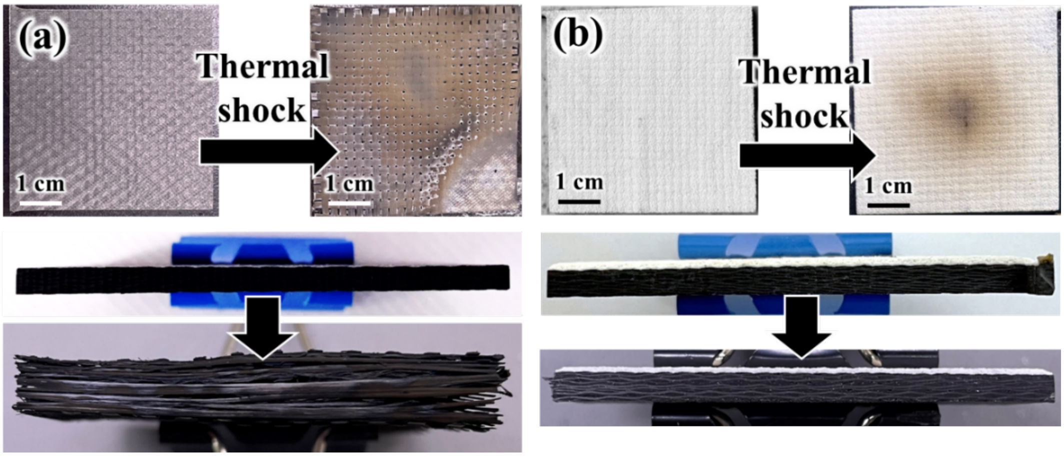

Figure 14. Macroscopic images of thermal shock-tested (a) pristine CFRP and (b) TBC/CFRP composites.

3.4. Residual Mechanical Performance of TBC/CFRP Composites

A series of three-point bending tests were performed to evaluate the residual mechanical properties of the TBC/CFRP composites. Figure 15 shows the representative flexural responses of TBC/CFRP composites before and after the thermal shock test (T_H = 500°C). Flexural tests were performed with tension on the CFRP composite side and compression on the TBC side. The thermal shock reduced the flexural strength and flexural modulus of the TBC/CFRP composite by 13% and 25%, respectively, as shown in Fig. 16. For instance, the pristine TBC/CFRP composite had a flexural strength of 348 MPa, but after a thermal shock test, its flexural strength was reduced to 302 MPa. The primary reason for flexural property degradation is the thermal decomposition of the epoxy matrix during the thermal shock. A distinct kink point in the stress-strain curve (marked by the black arrow) indicates the delamination between the desized CF substrate and the underlying CFRP composite. The flame-sprayed YSZ layer was well intact with the desized CF substrate, indicating good adhesion. The reduction in flexural modulus is due to oxygen vacancies formed in the double-layered TBC, during the thermal shock test. At high temperatures, these oxygen vacancies move within the lattice structure, increasing internal friction and damping and simultaneously decreasing elastic modulus [69].

The pristine CFRP composite showed flexural strength and modulus of 512 MPa and 29 GPa. Note that the pristine CFRP composites subjected to the thermal shock (T_H = 500°C) were burned and lost their structural stability (Fig. 13), thus the flexural test results of CFRP composites after a thermal shock was not feasible, and thus are not included in Fig. 15. As mentioned earlier, the flexural strength of the TBC/CFRP specimen (348 MPa) was lower than that of the CFRP specimen (512 MPa). This is due to the thickness and brittleness of the ceramic double-layered TBC. The TBC underwent compressive stress failure and damaged the adjacent CFRP layer, promoting crack propagation and decreasing the flexural strength of TBC/CFRP composites [70]. As mentioned eariler, the strength reduction of the thermal-shock-tested TBC/CFRP composites, observed at the kink in the flextural stress–strain curve (Fig. 15) was due to the thermal decomposition of the epoxy matrix at the interface of the CFRP and TBC layer. The flexure test results demonstrate that a double-layered TBC layer produced from the flame spraying can effectively mitigate thermal damage in the underlying CFRP composite without much loss in their mechanical properties, efficiently protecting the CFRP relative to its thickness.

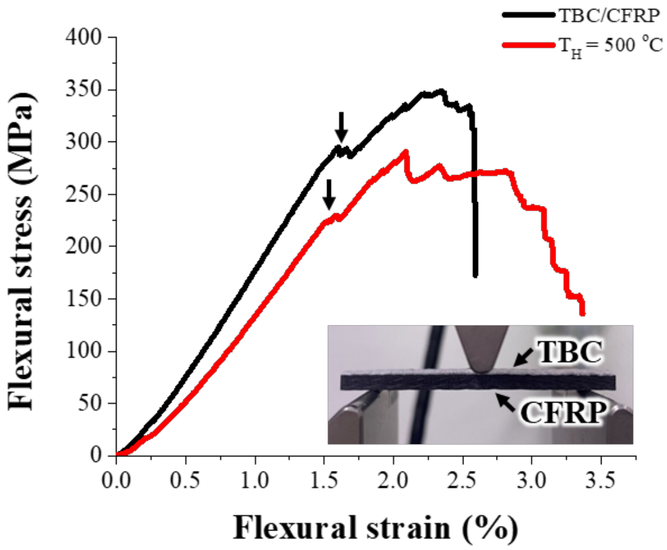

Figure 15. Flexural stress-strain curve of TBC/CFRP composites before and after thermal shock test (T_H = 500°C).

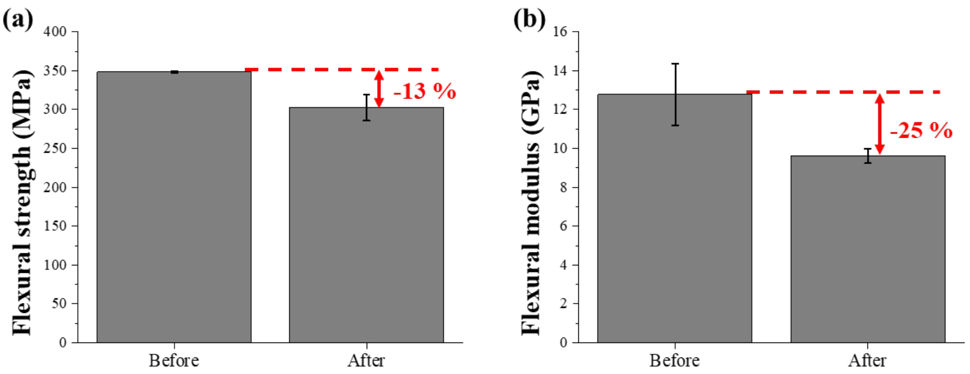

Figure 16. Comparison of (a) flexural strength and (b) flexural modulus of TBC/CFRP specimen after thermal shock (T_H = 500°C).

Cross-sectional microstructural images of TBC/CFRP before and after the thermal shock test and flexural test are shown in Fig. 17. For both as-prepared TBC/CFRP composite (Fig. 17a) and thermal-shocked TBC/CFRP composite (Fig. 17b), the interface between the TBC layer and underlying CFRP composite was well intact with each other. In general, the coefficient of thermal expansion (CTE) mismatch between the TBC and CFRP substrate greatly influences the failure at the interfaces [71]. However, such delamination was not observed because the working temperature was not as high as the YSZ operating temperature (1,200°C). Figure 17 also shows that the first CFRP ply holds good adhesion with the TBC layer. However, the interface between the underlying CFRP laminate and desized CF substrate coated with a double-layered YSZ layer is relatively as the desized CF has a non-polar surface, which hampers adhesion to the matrix [72]. Additionally, the high viscosity of partially cured epoxy made precipitation difficult. It is responsible for the first delamination indicated kink point in Fig. 15. In the tensile bonding test result of dense TBC/CFRP composites, the average adhesion strength was 5.45±0.5 MPa, the fracture occurred at the first CFRP ply (black region), and at the dense YSZ layer (white) as shown in Fig. S1. In the figures, the black region in the fracture interface was larger in area than the white region. This means that the adhesion between epoxy and desized CF is relatively weaker than the interfacial adhesion between CF and the YSZ layer.

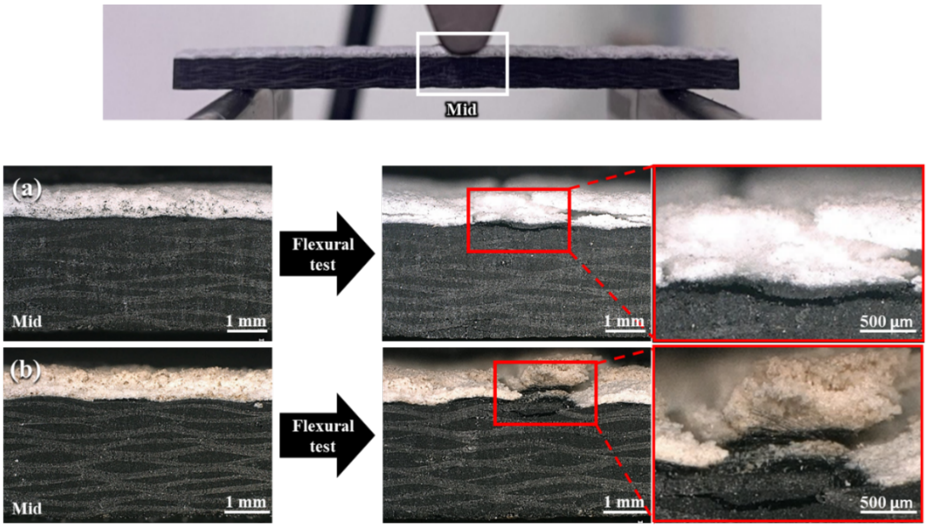

Figure 17. Cross-sectional images of TBC/CFRP specimens before and after three-point bending test. (a) before and (b) after thermal shock test.

4. Conclusion

This study proposes a double-layered thermal barrier coating (TBC) comprising dense and porous yttria-stabilized zirconia (YSZ) TBC layers fabricated directly onto dry CF substrate, followed by carbon fiber reinforced plastic (CFRP) fabrication. The thermal barrier performance and mechanical properties of TBC/CFRP composite were evaluated. The conclusions of this study are as follows:

1. A series of double-layered TBCs with graded density and porosity were produced by flame-spraying of YSZ and sacrificial polyetheretherketone (PEEK) powders, and the effects of flame spray process parameters on density, porosity, and thermal conductivity were characterized for optimal thermal barrier performance.

2. Thermal conductivity of the double-layered TBC decreased as both PEEK injection distance D and rate R increased, ensuring improved thermal barrier performance. The TBC fabricated with $D = 5$ cm and $R = 1.0$ g/min offered optimal thermal barrier performance and structural stability.

3. After the thermal shock test with flame temperature $T_H = 500°C$, the pristine CFRP composite was burned after 300 s, while the surface temperature of the underlying CFRP composite T_{CFRP} remained below 230°C up to 600 s without visual structural damage.

4. The TBC/CFRP composite retained 87% of its flexural strength and 75% of its flexural modulus after the thermal shock test.

This study explores the use of flame spraying to develop highly effective double-layered TBCs and to optimize their thermal barrier performances. The proposed TBC manufacturing method is simple and cost-effective compared to conventional porous ceramic TBC fabrication methods, allowing for the rapid formation of large-area coatings. Additionally, using vacuum-assisted resin transfer molding (VARTM) to manufacture TBC/CFRP composite leverages existing industrial processes. This suggests a high potential for other industrial applications. All findings from the present work provide new insights into the design and development of TBCs for CFRP composites, which may be immediately applied to firefighting and electric car battery housing materials. Furthermore, if other properties (*i.e.*, wear and corrosion resistance) of the TBC fabricated with the proposed flame spraying process are confirmed, this approach could benefit a wide range of high-temperature engineering applications, including aeronautical, aerospace, and military components.

Acknowledgments

This work was funded by the Korea Institute of Science and Technology (KIST) Institutional Program and the cooperation program between Forschungszentrum Jülich and the National Research Council of Science and Technology. This work was partially supported by the 2023 Hanwha Non-Tenured Faculty Award.

References

[1] Holmes M. Carbon fibre reinforced plastics market continues growth path. Reinforced plastics. 2013;57(6):24-9.
[2] Taynton P, Ni H, Zhu C, Yu K, Loob S, Jin Y, et al. Repairable woven carbon fiber composites with full recyclability enabled by malleable polyimine networks. Advanced Materials. 2016;28(15):2904-9.
[3] Forintos N, Czigany T. Multifunctional application of carbon fiber reinforced polymer composites: Electrical properties of the reinforcing carbon fibers–A short review. Composites Part B: Engineering. 2019;162:331-43.
[4] Bester N, Yates A. Assessment of the operational performance of Fischer-Tropsch synthetic-paraffinic kerosene in a T63 gas turbine compared to conventional Jet A-1 fuel. Turbo Expo: power for Land, Sea, and air2009. p. 1063-77.
[5] Zheng L, Changbo L, Gaojun A, Chunhua X, Youjie Z, Lianling R, et al. Comparative study on combustion and explosion characteristics of high flash point jet fuel. Procedia Engineering. 2014;84:377-83.
[6] Tao Y, Lu K, Chen X, Mao S, Ding Y, Zhao Y. Experimental investigation on the temperature profile of large scale RP–5 aviation kerosene pool fire in an open space. Fuel.

2020;264:116852.
[7] Tokyo plane crash puts carbon fiber materials under scrutiny. NIKKEI ASIA2024.
[8] Kodur V, Bhatt P, Naser M. High temperature properties of fiber reinforced polymers and fire insulation for fire resistance modeling of strengthened concrete structures. Composites Part B: Engineering. 2019;175:107104.
[9] Gadow R, Speicher M. Advanced Manufacturing of Ceramic Matrix Composites for Disk Brake Rotors. SAE Technical Paper; 2003.
[10] Sciti D, Galizia P, Reimer T, Schoberth A, Gutiérrez-Gonzalez C, Silvestroni L, et al. Properties of large scale ultra-high temperature ceramic matrix composites made by filament winding and spark plasma sintering. Composites Part B: Engineering. 2021;216:108839.
[11] Kim S-B, Kim S-H, Cho J-W. High temperature endurable metal matrix composite reinforced with continuously networked TiN. Journal of Alloys and Compounds. 2021;889:161633.
[12] Lima RS. Porous APS YSZ TBC manufactured at high powder feed rate (100 g/min) and deposition efficiency (70%): microstructure, bond strength and thermal gradients. Journal of Thermal Spray Technology. 2022;31(3):396-414.
[13] Liu B, Liu Y, Zhu C, Xiang H, Chen H, Sun L, et al. Advances on strategies for searching for next generation thermal barrier coating materials. Journal of Materials Science & Technology. 2019;35(5):833-51.
[14] Soleimanipour Z, Baghshahi S, Shoja-razavi R, Salehi M. Hot corrosion behavior of Al2O3 laser clad plasma sprayed YSZ thermal barrier coatings. Ceramics International. 2016;42(15):17698-705.
[15] Urbina M, Rinaldi A, Cuesta-Lopez S, Sobetkii A, Slobozeanu AE, Szakalos P, et al. The methodologies and strategies for the development of novel material systems and coatings for applications in extreme environments-a critical review. Manufacturing Review. 2018;5.
[16] Tejero-Martin D, Rezvani Rad M, McDonald A, Hussain T. Beyond traditional coatings: a review on thermal-sprayed functional and smart coatings. Journal of Thermal Spray Technology. 2019;28:598-644.
[17] Kumar S, Kumar R. Influence of processing conditions on the properties of thermal sprayed coating: a review. Surface Engineering. 2021;37(11):1339-72.
[18] Nicholls JR, Lawson K, Johnstone A, Rickerby D. Low thermal conductivity EB-PVD thermal barrier coatings. Materials science forum: Trans Tech Publ; 2001. p. 595-606.
[19] Bose S. High temperature coatings: Butterworth-Heinemann; 2017.
[20] Voyer J, Schulz P, Schreiber M. Electrically conductive flame sprayed aluminum coatings on textile substrates. Journal of thermal spray technology. 2008;17(5):818-23.
[21] Mostaghimi J, Pershin L, Salimijazi H, Nejad M, Ringuette M. Thermal spray copper alloy coatings as potent biocidal and virucidal surfaces. Journal of Thermal Spray Technology. 2021;30:25-39.
[22] Brobbey KJ, Haapanen J, Tuominen M, Mäkelä J, Gunell M, Eerola E, et al. High-speed production of antibacterial fabrics using liquid flame spray. Textile research journal. 2020;90(5-6):503-11.
[23] Voyer J. Flexible and conducting metal-fabric composites using the flame spray process for the production of Li-ion batteries. Journal of thermal spray technology. 2013;22:699-709.
[24] Gupta G, Tyagi R, Rajput S, Maan R, Jacob S, Verma S. Review on thermal spray coating methods and property of different types of metal-based coatings. Advances in Engineering Materials: Select Proceedings of FLAME 2020: Springer; 2021. p. 427-39.
[25] Govande AR, Chandak A, Sunil BR, Dumpala R. Carbide-based thermal spray coatings: A review on performance characteristics and post-treatment. International Journal of Refractory Metals and Hard Materials. 2022;103:105772.

[26] Łatka L, Pawłowski L, Winnicki M, Sokołowski P, Małachowska A, Kozerski S. Review of functionally graded thermal sprayed coatings. Applied Sciences. 2020;10(15):5153.

[27] Lima RS. Perspectives on thermal gradients in porous ZrO2-7–8 wt.% Y2O3 (YSZ) thermal barrier coatings (TBCs) manufactured by air plasma spray (APS). Coatings. 2020;10(9):812.

[28] Xie P, Chen J, Ye B, Wang R, Dang K, Yang W, et al. Plasma sprayed thermal barrier coatings: Effects of polyamide additive on injection molding part quality. Journal of Applied Polymer Science. 2022;139(16):51980.

[29] Sun F, Fan X, Zhang T, Jiang P, Yang J. Numerical analysis of the influence of pore microstructure on thermal conductivity and Young's modulus of thermal barrier coating. Ceramics International. 2020;46(15):24326-32.

[30] Lv B, Fan X, Li D, Wang T. Towards enhanced sintering resistance: Air-plasma-sprayed thermal barrier coating system with porosity gradient. Journal of the European Ceramic Society. 2018;38(4):1946-56.

[31] Krishnaswamy S, Abhyankar H, Marchante V, Huang Z, Brighton J. Aerogel/epoxy thermal coatings for carbon fibre reinforced plastic substrates. Journal of Adhesion Science and Technology. 2019;33(6):579-94.

[32] Luangtriratana P, Kandola BK, Myler P. Ceramic particulate thermal barrier surface coatings for glass fibre-reinforced epoxy composites. Materials & Design. 2015;68:232-44.

[33] Golewski P, Sadowski T. A novel application of alumina fiber mats as TBC protection for CFRP/epoxy laminates–Laboratory tests and numerical modeling. Journal of the European Ceramic Society. 2018;38(8):2920-7.

[34] Cilento F, Leone C, Genna S, Giordano M, Martone A. Graphene NanoPlatelet-based coating as thermal protection from high-power radiative fluxes. Composite Structures. 2023;319:117157.

[35] Ju L, Yang J, Hao A, Daniel J, Morales J, Nguyen S, et al. A hybrid ceramic-polymer composite fabricated by co-curing lay-up process for a strong bonding and enhanced transient thermal protection. Ceramics International. 2018;44(10):11497-504.

[36] Kopeliovich D. Advances in the manufacture of ceramic matrix composites using infiltration techniques. Advances in ceramic matrix composites: Elsevier; 2014. p. 79-108.

[37] Kim H, Kim J, Lee J, Lee MW. Thermal barrier coating for carbon fiber-reinforced composite materials. Composites Part B: Engineering. 2021;225:109308.

[38] Moridi A, Azadi M, Farrahi G. Thermo-mechanical stress analysis of thermal barrier coating system considering thickness and roughness effects. Surface and Coatings Technology. 2014;243:91-9.

[39] Clarke DR, Phillpot SR. Thermal barrier coating materials. Materials today. 2005;8(6):22-9.

[40] Lee KN, Fox DS, Eldridge JI, Zhu D, Robinson RC, Bansal NP, et al. Upper temperature limit of environmental barrier coatings based on mullite and BSAS. Journal of the American Ceramic Society. 2003;86(8):1299-306.

[41] Nicholls JR, Lawson K, Johnstone A, Rickerby DS. Methods to reduce the thermal conductivity of EB-PVD TBCs. Surface and Coatings Technology. 2002;151:383-91.

[42] Zhao H, Yu F, Bennett TD, Wadley HN. Morphology and thermal conductivity of yttria-stabilized zirconia coatings. Acta materialia. 2006;54(19):5195-207.

[43] Hu L, Wang C-A, Huang Y, Sun C, Lu S, Hu Z. Control of pore channel size during freeze casting of porous YSZ ceramics with unidirectionally aligned channels using different freezing temperatures. Journal of the European Ceramic Society. 2010;30(16):3389-96.

[44] KUKDO. G-640 Polyamide Resin. 2004.

[45] (ASTM) ASfTaM. Standard Test Methods for Determination of Water Absorption and

Associated Properties by Vacuum Method for Pressed Ceramic Tiles and Glass Tiles and Boil Method for Extruded Ceramic Tiles and Non-tile Fired Ceramic Whiteware Products. 2018. p. 6.
[46] Standard A. Standard test methods for flexural properties of unreinforced and reinforced plastics and electrical insulating materials. ASTM D790. Annual book of ASTM standards. 1997.
[47] (ASTM) ASfTaM. Standard Test Method for Adhesion or Cohesion Strength of Thermal Spray Coatings. 2021. p. 8.
[48] Fanicchia F, Axinte D, Kell J, McIntyre R, Brewster G, Norton A. Combustion flame spray of CoNiCrAlY & YSZ coatings. Surface and Coatings Technology. 2017;315:546-57.
[49] Mendoza MV, Alvarez RC, Juarez Lopez F. Combustion flame spray of 7YSZ powders followed by corrosion in molten salts of the coating. Journal of Asian Ceramic Societies. 2021;9(2):617-28.
[50] Portinha A, Teixeira V, Carneiro J, Martins J, Costa M, Vassen R, et al. Characterization of thermal barrier coatings with a gradient in porosity. Surface and coatings technology. 2005;195(2-3):245-51.
[51] Meierhofer F, Mädler L, Fritsching U. Nanoparticle evolution in flame spray pyrolysis—Process design via experimental and computational analysis. AIChE Journal. 2020;66(2):e16885.
[52] Khelfi D, El-Hadj AA, Aït-Messaoudène N. Modeling of a 3D plasma thermal spraying and the effect of the particle injection angle. Revue des Energies Renouvelables CISM. 2008;8:205-16.
[53] Olson DH, Deijkers JA, Quiambao-Tomko K, Gaskins JT, Richards BT, Opila EJ, et al. Evolution of microstructure and thermal conductivity of multifunctional environmental barrier coating systems. Materials Today Physics. 2021;17:100304.
[54] Wang J, Chong X, Zhou R, Feng J. Microstructure and thermal properties of RETaO4 (RE= Nd, Eu, Gd, Dy, Er, Yb, Lu) as promising thermal barrier coating materials. Scripta Materialia. 2017;126:24-8.
[55] Huang Y, Hu N, Zeng Y, Song X, Lin C, Liu Z, et al. Effect of different types of pores on thermal conductivity of YSZ thermal barrier coatings. Coatings. 2019;9(2):138.
[56] Feuerstein A, Knapp J, Taylor T, Ashary A, Bolcavage A, Hitchman N. Technical and economical aspects of current thermal barrier coating systems for gas turbine engines by thermal spray and EBPVD: a review. Journal of Thermal Spray Technology. 2008;17(2):199-213.
[57] Bobzin K, Zhao L, Öte M, Königstein T. A highly porous thermal barrier coating based on Gd2O3–Yb2O3 co-doped YSZ. Surface and Coatings Technology. 2019;366:349-54.
[58] Curry N, Leitner M, Körner K. High-porosity thermal barrier coatings from high-power plasma spray equipment—processing, performance and economics. Coatings. 2020;10(10):957.
[59] Jiang C. Low Thermal Conductivity YSZ-based Thermal Barrier Coatings with Enhanced CMAS Resistance: University of Connecticut; 2015.
[60] Łatka L, Cattini A, Pawłowski L, Valette S, Pateyron B, Lecompte J-P, et al. Thermal diffusivity and conductivity of yttria stabilized zirconia coatings obtained by suspension plasma spraying. Surface and Coatings Technology. 2012;208:87-91.
[61] Ganvir A, Curry N, Björklund S, Markocsan N, Nylén P. Characterization of microstructure and thermal properties of YSZ coatings obtained by axial suspension plasma spraying (ASPS). Journal of Thermal Spray Technology. 2015;24:1195-204.
[62] Bernard B, Quet A, Bianchi L, Joulia A, Malié A, Schick V, et al. Thermal insulation properties of YSZ coatings: suspension plasma spraying (SPS) versus electron beam physical

vapor deposition (EB-PVD) and atmospheric plasma spraying (APS). Surface and Coatings Technology. 2017;318:122-8.
[63] Mittal G, Paul S. Suspension and solution precursor plasma and HVOF spray: A review. Journal of Thermal Spray Technology. 2022;31(5):1443-75.
[64] Lee J, Lacy Jr TE, Pittman Jr CU, Mazzola MS. Temperature-dependent thermal decomposition of carbon/epoxy laminates subjected to simulated lightning currents. Polymer Composites. 2018;39(S4):E2185-E98.
[65] Lee J, Lacy Jr TE, Pittman Jr CU, Mazzola MS. Thermal response of carbon fiber epoxy laminates with metallic and nonmetallic protection layers to simulated lightning currents. Polymer Composites. 2018;39(S4):E2149-E66.
[66] Dennison PE, Charoensiri K, Roberts DA, Peterson SH, Green RO. Wildfire temperature and land cover modeling using hyperspectral data. Remote Sensing of Environment. 2006;100(2):212-22.
[67] ui Lee X. Introduction to wildland fire: by SJ Pyne, PL Andrews and RD Laven, John Wiley and Sons, Chichester, UK, 1996, 769 pp.,£ 70.00, ISBN 0-471-54913-4. Elsevier; 1997.
[68] Morvan D, Dupuy J-L. Modeling the propagation of a wildfire through a Mediterranean shrub using a multiphase formulation. Combustion and flame. 2004;138(3):199-210.
[69] Radovic M, Lara-Curzio E, Trejo RM, Wang H, Porter W. Thermophysical Properties of YSZ and Ni-YSZ as a Function of Temperature and Porosity. Advances in solid oxide fuel cells II: ceramic engineering and science proceedings. 2006;27:79-85.
[70] Caliskan H, Panjan P, Kurbanoglu C. Hard coatings on cutting tools and surface finish. 2017.
[71] Hutchinson J, Evans A. On the delamination of thermal barrier coatings in a thermal gradient. Surface and Coatings Technology. 2002;149(2-3):179-84.
[72] Wu Q, Zhao R, Zhu J, Wang F. Interfacial improvement of carbon fiber reinforced epoxy composites by tuning the content of curing agent in sizing agent. Applied Surface Science. 2020;504:144384.